Numerical and Experimental Investigation of Shock Waves in Hypersonic Axisymmetric Jets

I.A. Graur[1], T.G. Elizarova[1], A. Ramos[2], G. Tejeda[2], J.M. Fernández[2], and S. Montero[2⋆]

[1] Institute for Mathematical Modeling, Russian Academy of Sciences, Miusskaya Square 4a, 125047 Moscow, Russia
[2] Instituto de Estructura de la Materia, CSIC, Serrano 121, 28006 Madrid, Spain

Abstract. A comprehensive numerical and experimental study of hypersonic normal shock waves in steady axisymmetric jets of N_2 is presented. The numerical interpretation is based on the quasigasdynamic (QGD) approach, and its generalization (QGDR) for the breakdown of rotational–translational equilibrium. The experimental part, based on diagnostics by high sensitivity Raman spectroscopy, provides absolute density and rotational temperatures along the expansion axis, the wake beyond the shock included. A general structure is found consisting of a nearly planar hypersonic shock wave preceding a subsonic encapsulated vortex which acts as an obstacle in the flow.

1 Introduction

A number of earlier works on supersonic gas dynamics has reported the basic theory [1–5] and several experimental results [6–9] on shock waves. Most of these studies were however restricted to the somewhat idealized one-dimensional (1D) problem, relatively far apart from practical cases. Taking advantage of recent theoretical and experimental developments here we present a comprehensive preliminary survey of the two-dimensional (2D) problem of shock waves generated in axisymmetric jets of N_2 covering the Mach number range $7.7 \leq M \leq 15.3$. The peculiarities of the 1D problem remain, more or less modified, in the 2D problem, as for instance, the sharp density and temperature gradients across the shock, the breakdown of translational–rotational thermal equilibrium, the lag between density, rotational temperature, and translational temperature profiles, the thermal overshoot at the end of the shock wave, and the bimodal distribution of temperatures. But other features, like the formation of a trapped vortex immediately after the shock wave, appear to be proper of the 2D problem. An overview of the 2D axisymmetric normal shock waves is presented next.

2 Theory

The numerical interpretation is based on the quasigasdynamic (QGD) system of equations, and its generalization (QGDR) considering the translational–

⋆ EMail: emsalvador @ iem.cfmac.csic.es

rotational breakdown of thermal equilibrium. QGD equations have been constructed and investigated as an extension of the traditional Navier–Stokes (NS) equations. QGD equations reduce to NS equations for vanishing Knudsen numbers. An example of the application of the QGD and QGDR systems to underexpanded jet modelling has been reported recently [10].

The translational–rotational nonequilibrium in a gas with two rotational degrees of freedom can be accounted for by means of the QGDR system of equations [11]

$$\frac{\partial}{\partial t}\rho + \nabla_i \rho u^i - \nabla_i \tau(\nabla_j \rho u^i u^j + \nabla^i p_{tr}) = 0, \tag{1}$$

$$\frac{\partial}{\partial t}\rho u^k + \nabla_i \rho u^i u^k + \nabla^k p_{tr} = \nabla_i \tau \nabla_j \rho u^i u^j u^k + \nabla_i \tau(\nabla^i p_{tr} u^k + \nabla^k p_{tr} u^i) + \nabla^k \tau \nabla_i p_{tr} u^i, \tag{2}$$

$$\frac{\partial}{\partial t}E_{tr} + \nabla_i u^i (E_{tr} + p_{tr}) = \nabla_i \tau \left[\nabla_j (E_{tr} + 2p_{tr}) u^i u^j + \frac{1}{2}\nabla^i u_k u^k p_{tr}\right] + \frac{5}{2}\nabla_i \tau \frac{p_{tr}}{\rho}\nabla^i p_{tr} + Pr^{-1}\frac{5}{2}\nabla_i \tau p_{tr}\nabla^i \frac{p_{tr}}{\rho} + S_{tr}, \tag{3}$$

$$\frac{\partial}{\partial t}E_{rot} + \nabla_i u^i E_{rot} = \nabla_i \tau \nabla_j u^i u^j E_{rot} + \nabla_i \tau \frac{p_{rot}}{\rho}\nabla^i p_{tr} + Pr^{-1}\nabla_i \tau p_{tr}\nabla^i \frac{p_{rot}}{\rho} + S_{rot}, \tag{4}$$

where the macroscopic flow quantities are density ρ, velocity u_i pressure p and

$$E_{tr} = (\rho u_i^2)/2 + 3p_{tr}/2, \quad E_{rot} = p_{rot}, \tag{5}$$

with $p_{tr} = \rho(\mathcal{R}/\mathcal{M})T_{tr}$, $p_{rot} = \rho(\mathcal{R}/\mathcal{M})T_{rot}$; $\mathcal{R}$ is the universal gas constant, $\mathcal{M}$ the molar mass of the gas, Pr is Prandtl number and $\tau = \mu/p_{tr}$ is a relaxation time related to the gas viscosity. The viscosity coefficient has been treated within the variable hard sphere (VHS) model, which leads to a thermal dependence

$$\mu = \mu_{ref}\,(T_{tr}/T_{ref})^{\omega}\,. \tag{6}$$

For N_2, $\omega = 0.74$ and $\mu_{ref} = 1.656 \times 10^{-5}$ N·s m^{-2} at $T_{ref} = 273$ K [12]. The translational–rotational energy exchange terms are defined by

$$S_{tr} = -S_{rot} = \frac{3}{5\tau_{rot}}(p_{rot} - p_{tr}), \tag{7}$$

where the rotational relaxation time τ_{rot} can be estimated as $\tau_{rot} = Z\tau_c$; $\tau_c = \tau(7 - 2\omega)(5 - 2\omega)/30$ is the mean collisional time, and

$$Z = \frac{Z^{\infty}}{1 + (\pi^{3/2}/2)(T^{\star}/T_{tr})^{1/2} + (\pi + \pi^2/4)(T^{\star}/T_{tr})} \tag{8}$$

is the so-called rotational collision number. The parameters $Z^{\infty} = 23$ and $T^{\star} = 91.5$ K have been used here for N_2 [12].

Average pressure and temperature derived from the QGDR generalization, to be compared to the homologous QGD quantities, p and T, are defined as

$$p_{av} = (3\,p_{tr} + 2\,p_{rot})/5 = \rho\,(\mathcal{R}/\mathcal{M})\,T_{av}. \tag{9}$$

At thermal equilibrium $p_{tr} = p_{rot} = p_{av} = p$ and

$$E = E_{tr} + E_{rot} = \frac{\rho u_i^2}{2} + \frac{p}{\gamma - 1}, \tag{10}$$

the QGDR system turning into the one-temperature QGD system with specific heat ratio $\gamma = (5+\xi)/(3+\xi) = 7/5$ for a non-monatomic gas with $\xi = 2$ internal degrees of freedom.

The QGDR system of equations, adapted to (z, r) axisymmetric coordinates, is solved here numerically using a finite–difference algorithm of second-order in space, with the steady-state attained as the limit of a time evolving process [10]. Nozzle exit quantities employed in the calculation are given in Table 1, where the subscripts e and ∞ refer to nozzle exit and the expansion background conditions respectively.

Table 1. Nozzle exit quantities of the N_2 jet employed in the QGDR numerical runs

M_e	1.01	$Kn_e = \lambda_e/D$	3.75×10^{-4}
T_e	249.2 K	T_∞/T_e	200/249.2
p_e	0.382 bar	p_∞/p_e	(A) 0.0110
n_e	1.1114×10^{25} m^{-3}		(B) 0.00262
ρ_e	0.517 kg m^{-3}		(C) 0.00131
u_e	325.0 ms^{-}1		(D) 0.000732
λ_e	11.73×10^{-8} m		(E) 0.000471

3 Experiment

The density and rotational temperature profiles of the normal shock waves investigated here have been measured by means of Raman spectroscopy according to the procedure described elsewhere [13,14] (see also contribution 2244 to ISSW23). Five reference shock waves were generated by expansion of N_2 through a nozzle of exit diameter $D = 313$ μm and internal length ≈ 1 mm, under nominal stagnation pressure $p_0 = 1$ bar and temperature $T_0 = 295$ K. These shock waves, henceforth referred to as A, B, C, D and E, are located at reduced distances to the nozzle, $\tilde{z} = z/D \approx 9$, 18, 27, 36, and 45. The locations were fixed by the ratios of stagnation to residual pressure p_0/p_∞, for $p_\infty = 4.2$, 1, 0.5, 0.28

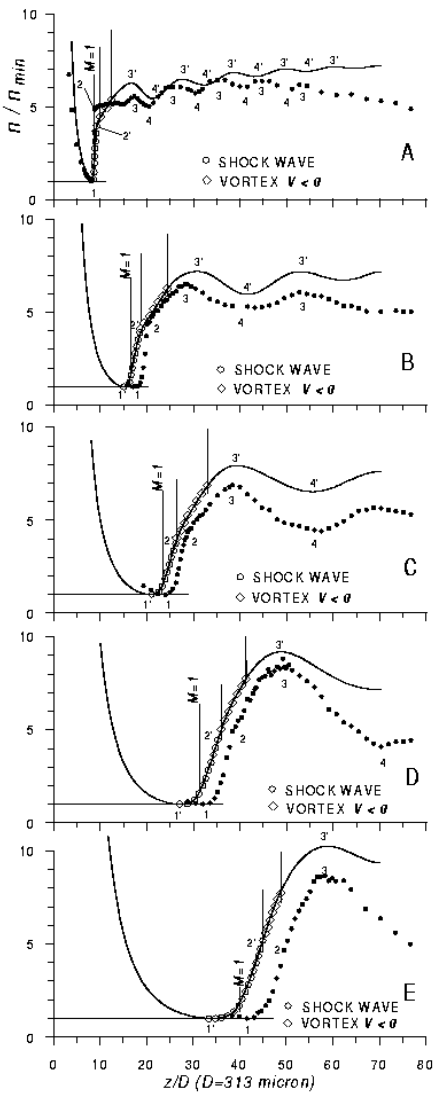

Fig. 1. Experimental (•) and QGDR calculated (—,○,◇) axial density profiles of N_2 normal shock waves

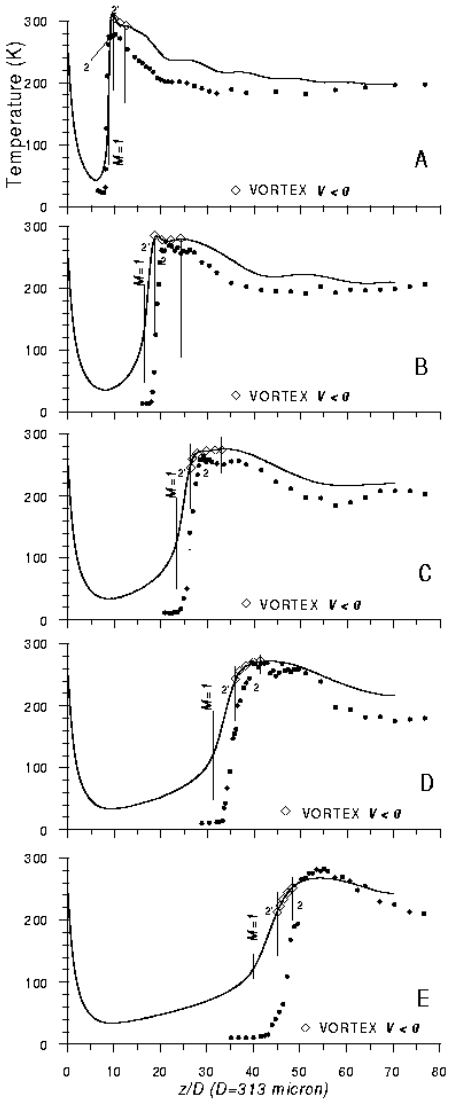

Fig. 2. Experimental (•) and QGDR calculated (—,◇) axial rotational temperature profiles of N_2 normal shock waves

and 0.18 mb, respectively, controlling the residual pressure by means of an inlet needle valve in the expansion chamber. The experimental density and rotational temperature profiles of shock waves A, B, ..., E, are shown in Figs. 1 and 2, jointly with the QGDR calculated counterparts.

3.1 Density and Temperature Profiles

In Fig. 1, the experimental density profiles of the expansions A, B, ..., E show a systematic trend characterized by a discontinuity in the slope of the density, labeled as point 2. As shown in Fig. 2, this discontinuity coincides, to experimental accuracy, with the rethermalization of the rotational temperature to about nozzle exit temperature, $T_e = 249$ K. The actual shock wave appears to extend from a point located slightly upstream from point 1, of minimum density upstream of the shock, to point 2, of rotational rethermalization.

The density jump attributed to the shock, between points 2 and 1, is found to obey the relation

$$\frac{n_2}{n_1} = \left(\frac{z_1}{z_2}\right)^2 \frac{(\gamma+1)M^2}{2+(\gamma-1)M^2}, \tag{11}$$

where $M \approx 7.7$, 10.6, 12.2, 13.6, and 15.3, is the Mach number at the onset of shocks A, B, ..., E, respectively; M values have been estimated from the distance between shock wave and nozzle according to an empirical parametrization [15]. In the limit of infinitesimal width ($\tilde{z}_2 = \tilde{z}_1$), (11) leads to the Rankine–Hugoniot density jump across an ideal monodimensional shock wave. For increasingly larger widths $\delta \propto (\tilde{z}_2 - \tilde{z}_1)$ of the shock wave, that is, for larger degrees of rarefaction and mean free path, the discontinuity in the gradient of density at point 2 tends to vanish. In shock wave E, it is no longer evident (recognizable), as shown in Fig. 1, but its location can be inferred approximately from the rethermalization of rotational temperature, shown in Fig. 2.

QGDR calculated density profiles also predict a change in the density gradient at points $2'$, close to the experimental points 2, but this change is far smoother than observed in the experiment. With exception of shock wave A, calculated points $2'$ are somewhat closer (≈ 10 percent) to the nozzle than the experimental ones. Points $2'$ seem to be related with the boundary of an encapsulated vortex located immediately after the shock wave, since the axial flow velocity V becomes negative immediately beyond point $2'$, and returns to a positive value prior to the first point $3'$. In Figs. 1 and 2 the calculated shock wave region is marked by circles ($\circ$), while vortex is marked with diamonds ($\diamond$). Experimental points 2, obviously correlated with calculated points $2'$, appear to provide an experimental sign of vortex onset.

Between points 2 and 3 the density gradient is positive, but smaller than at the shock, and at point 3 the density reaches a local maximum. Beyond that point a secondary expansion is observed, with a quasi-periodical structure of density maximum (point 3), and minimum (point 4). QGDR calculated density profiles in the wake beyond the normal shock, including the periodical structure of density maximum (point $3'$) and minimum (point $4'$), agree well with experiment, as shown in Fig. 1.

QGDR calculated rotational temperature profiles can be compared with experimental values in Fig. 2. For shock wave A at $M = 7.7$, the agreement is fairly good, although calculated temperatures are overestimated by about 25 K with respect to the experiment. For shocks B, ..., E at increasingly higher Mach numbers, calculated thermal profiles prior to the rethermalization point $2'$ depart

progressively from the experimental ones. The calculated onset of the rotational thermal shocks at $M > 8$ is poorly reproduced by the calculation, showing too large a lag between density and temperature minima. Corresponding experimental minima are much closer, and the experimental onset of thermal shock is far sharper. Whether this disagreement is due to an inadequate description of the viscosity at temperatures below 50 K, or is an inherent limitation of the QGDR approach at high Knudsen numbers, requires further investigation. Estimated maxima of local Knudsen numbers at shocks A, B, ..., E, are $Kn^{max} \approx 0.33$, 0.35, 0.42, 0.54, and 0.59, respectively. However, rethermalization after the shock is nicely reproduced by the QGDR calculation in all cases, a result of particular relevance since this region beyond the shock includes a zone of an encapsulated vortex which will be discussed next.

4 QGDR Flow Fields

In spite of the particular discrepancies mentioned above, a reasonable overall agreement between QGDR calculated and experimental density and rotational temperature profiles confers to the QGDR results a reasonable degree of credibility. QGDR results also include a complete representation of the flow field, which is summarized in Fig. 3. A striking feature of the calculated flow fields is the steady recirculation vortex trapped immediately after the shock wave. This vortex seems to be a general property associated with 2D normal shock waves.

A close scrutiny of Fig. 3, shown in more detail in Fig. 4 for case E, reveals that the vortex (subsonic) is separated from the main supersonic stream by a surface Σ where the normal and tangential components of velocity V_n and V_t to Σ satisfy the boundary conditions

$$V_n^+ = V_n^- = 0, \quad \text{(a)} \tag{12}$$

$$V_t^+ = V_t^- \neq 0, \quad \text{(b)} \tag{13}$$

superscripts + and − referring to the main stream and to the vortex region respectively. (a) and (b) are so a particular case of the stream function isolines. Condition (a) implies that Σ is a contact surface which does not propagate with respect to the surrounding flow, Σ actually behaves as a clockwise rotating obstacle encapsulated in the flow. The nature of point $2'$ of discontinuity in the density gradient (Fig. 1) and of rotational rethermalization (Fig. 2) becomes evident in Fig. 4, where point $2'$ marks the confluence of the main flow and of the counterpropagating axial section of the vortex. Merging of these two flows at the molecular scale appears to extend to the whole shock wave. Note that average bulk velocities are reported in Figs. 3 and 4, but individual molecules obey a bimodal velocity distribution centered at that average value. According to experiment (see also contribution 2244p to ISSW23) in this process each flow seems to maintain its individuality, although the proportion changes by interconversion. The main stream, of low density, supersonic speed, and low rotational temperature, vanishes in going along the expansion axis from point 1 to point

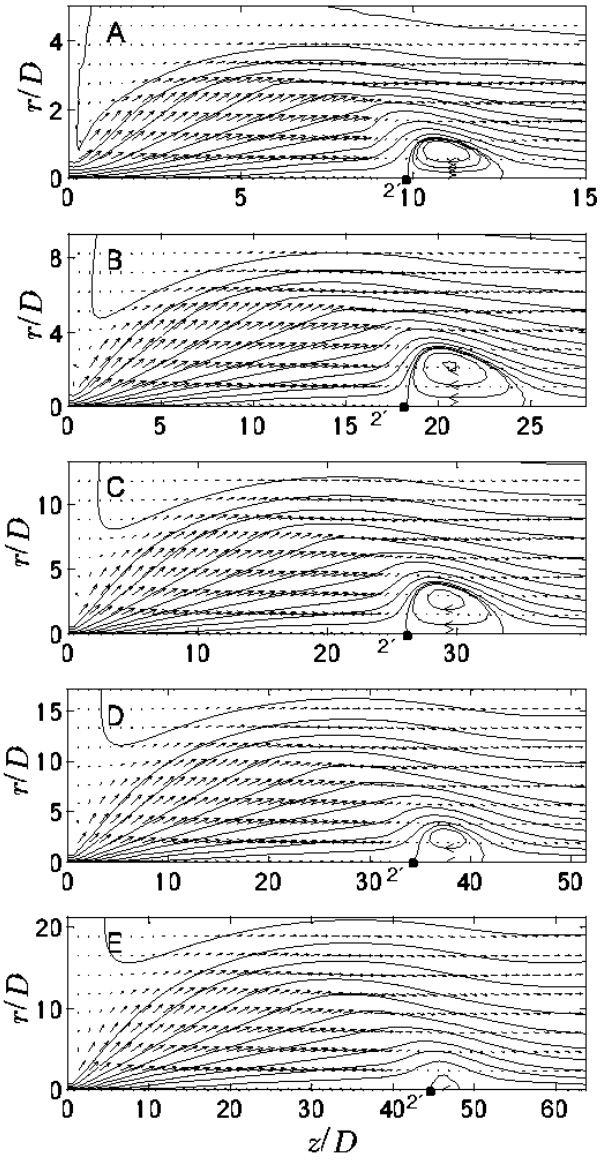

Fig. 3. QGDR calculated flow fields of N_2 expansions A, B, ..., E

2. The counterpropagating vortex flow, of high density, subsonic velocity, and rethermalized rotational temperature, vanishes in going in the opposite direction from point 2 to point 1. This picture is consistent with the bimodal model of temperatures [1], and still more consistent with the two-fluid model [3], in spite of both models having been derived for the 1D problem.

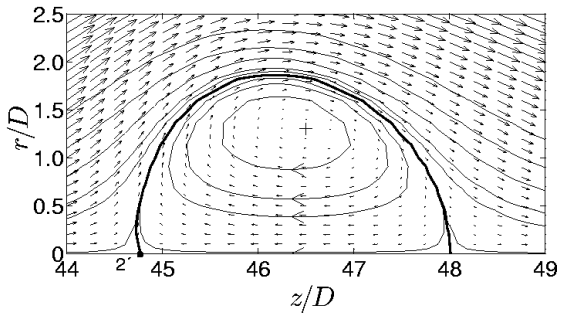

Fig. 4. Detail of the vortex (+) of expansion E according to QGDR calculation; Σ-surface marked with bold line

5 Conclusions

Present numerical and experimental results strongly suggest that the general structure of shocks associated with 2D axisymmetric supersonic jets is formed by a nearly planar normal shock wave followed by a recirculating trapped vortex. As far as the actual shock wave section of this complex structure is concerned, QGDR calculations appear unable to describe properly the bimodal thermal behavior observed in the experiment. This may well be due to its present formulation, based on an average flow velocity and a single rotational temperature at each point of the flow. In spite of this limitation, the QGDR approach appears capable of providing a reasonable global description of the 2D axisymmetric jet, especially for Mach numbers $M < 8$, and local Knudsen numbers $Kn^{max} \leq 0.33$.

The vortex described, of high density and low velocity, appears to be driven by the external barrel of the jet. The first experimental evidence of vortex onset is the discontinuity in the density gradient, marked in present work with points 2 (experiment) or $2'$ (calculation). Such points coincide with the rethermalization of the rotational temperature to nozzle exit temperature.

Acknowledgement. This work was supported by the Russian Foundation for Basic Research, grant N 01-01-00061, and by the Spanish DGESIC (MEC), research project PB97-1203.

References

1. Mott-Smith HM (1951) The solution of the Boltzmann equation for a shock wave. Phys Rev 82(6):885–892
2. Ziering S, Ek F, Koch P (1961) Two-fluid model for the structure of neutral shock waves. Phys Fluids 4(8):975–987
3. Glansdorff P (1962) Solution of the Boltzmann equation for strong shock waves by the two-fluid model. Phys Fluids 5(4):371–379
4. Muckenfuss C (1962) Some aspects of shock structure according to the bimodal model. Phys Fluids 5(11):1325–1336

5. Toba K, Melnick JD (1965) Two-fluid model for shock wave structure. Phys Fluids 8(12):2153–2157
6. Robben F, Talbot L (1966) Measurement of shock wave thickness by the electron beam fluorescence method. Phys Fluids 9(4):633–643; Experimental study of the rotational distribution function of nitrogen in a shock wave. Phys Fluids 9(4):653–662
7. Marrone PV (1967) Temperature and density measurements in free jets and shock waves. Phys Fluids 10(3):521–538
8. Alsmayer J (1976) Density profiles in argon and nitrogen shock waves measured by the absorption of an electron beam. J Fluid Mech 74:497–513
9. Pham-Van-Diep G, Erwin D, Muntz EP (1989) Nonequilibrium molecular motion in a hypersonic shock wave. Science 245:624–626
10. Maté B, Graur I, Elizarova T, Chirokov I, Tejeda G, Fernández JM, Montero S (2001) Experimental and numerical investigation of an axisymmetric supersonic jet. J Fluid Mech 426:177–197
11. Elizarova TG, Shirokov IA (1999) A macroscopic gas model with translational and rotational nonequilibrium. Comput Mathem and Mathem Phys 39(1):135–146
12. Bird GA (1994) Molecular gas dynamics and the direct simulation of gas flows. Oxford Univ Press, New York
13. Ramos A, Maté B, Tejeda G, Fernández JM, Montero S (2000) Raman spectroscopy of hypersonic shock waves. Phys Rev E 62(4):4940–4945
14. Montero S, Maté B, Tejeda G, Fernández JM, Ramos A (2000) Raman studies of free jet expansion. Diagnostics and mapping. In: *Atomic and Molecular Beams. The State of the Art, 2000*, ed¿ by R. Campargue, Springer, Berlin, 295–306
15. Miller DR (1988) Free jet sources. In: *Atomic and Molecular Beams Methods*, ed. by G. Scoles, Oxford Univ Press, New York, I:14–53